Nano Research

Open Access

Research Article

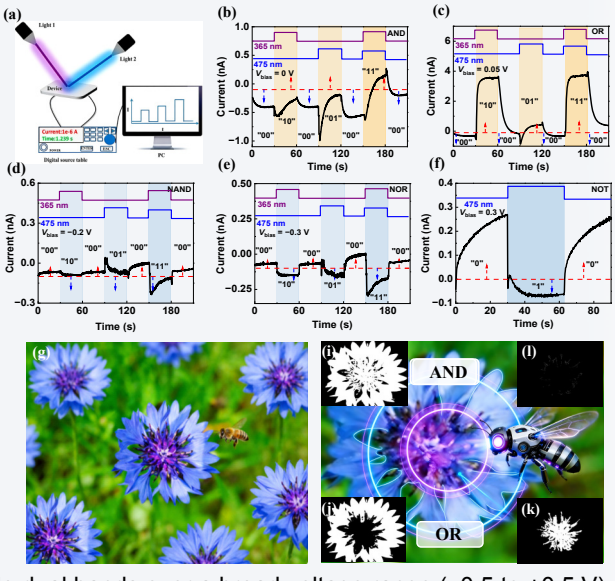
Wavelength-controlled bipolar photoresponse in BiOI/TiO_2 heterojunctions for reconfigurable optoelectronic logic gates and biomimetic in-sensor processing

Jianping Xu[1] ✉, Hongye An[1,2], Shaobo Shi[3], Lina Kong[2], Xiaosong Zhang[2], and Lan Li[2]

[1] *Tianjin Key Laboratory of Quantum Optics and Intelligent Photonics, School of Science, Tianjin University of Technology, Tianjin 300384, China*
[2] *School of Materials Science and Engineering, Key Laboratory of Display Materials and Photoelectric Devices, Ministry of Education, and Tianjin Key Laboratory for Photoelectric Materials and Devices, Tianjin University of Technology, Tianjin 300384, China*
[3] *School of Science, Tianjin University of Technology and Education, Tianjin 300222, China*

Cite this article: *Nano Research*, **2026**, *19*, 94908701. https://doi.org/10.26599/NR.2026.94908701

ABSTRACT: Optoelectronic logic gate devices (OELGD) utilizing photons as input signals hold great potential for high-speed, high-capacity data transmission and processing, offering a promising solution to the "electronic bottleneck" problem. Wavelength-controlled bipolar photoresponse photodetectors (PDs) are critical for advancing such as OELGDs. In this study, BiOI/TiO_2 heterojunctions were constructed by depositing two-dimensional layered BiOI nanoflakes onto TiO_2 thin film via a solvothermal method. Leveraging the large conduction-band and valence-band offsets of the heterojunction, wavelength-tunable dual-polarity photocurrent was achieved by modulating barrier tunneling and recombination processes of photo-generated carriers at the interface under ultraviolet (UV) and visible light illumination. The stoichiometric ratio of BiOI was adjusted by introducing glycerol during synthesis, which regulated the BiOI conduction-band position and consequently modulating the conduction-band offset of BiOI/TiO_2 heterojunction. The optimized heterojunction with 1 mL glycerol addition exhibited wavelength-controlled bipolar photoresponse across the UV–visible dual bands over a broad voltage range (–0.5 to +0.5 V). Using UV and visible light as input signals, five basic logic gates ("AND", "OR", "NAND", "NOR", and "NOT") were implemented in a single BiOI/TiO_2 heterojunction PDs. Furthermore, by harnessing this UV–visible logic functionality, in-sensor processing of *Chrysanthemum carinatum* images was realized, simulating the biological phenomenon where bees perceive UV nectar guides on flower petals that are invisible to humans. These results demonstrate the potential of BiOI/TiO_2 devices as innovative components for reconfigurable OELGDs.



KEYWORDS: BiOI, dual-band polarity, carrier tunneling/recombination, optoelectronic logic gate

1 Introduction

Logic gate serve as the fundamental building blocks of digital circuits, enabling logical operations on digital signals. The rapid development of information technologies such as the internet of things, big data, cloud computing, and artificial intelligence has created the urgent need for high-density, high-speed, and low-power logic devices [1–3]. Optical logic gate device (OLGD) with all-optical input/output and optoelectronic logic gate device (OELGD) with optical input/electrical output leverage photon transmission to achieve advantages such as high speed, large bandwidth, no Joule heating, and immunity to electromagnetic interference, thereby addressing the "electronic bottleneck"

Received: January 24, 2026; **Revised:** March 22, 2026
Accepted: April 1, 2026

✉Address correspondence to xjp0335@163.com

inherent in electronic logic gate device (ELGD) [4, 5]. Two primary approaches have been proposed to realize OLGDs: interference-based logic gates utilizing linear effects and logic gates exploiting nonlinear effects in optical media [6, 7]. While OLGDs can offer advantages such as optical gain, saturated output power, wide gain bandwidth, and rapid information processing, they often suffer from high component costs, large footprint, and strict placement requirements [4, 8, 9]. In contrast, OELGD based on emerging non-silicon materials can provide faster data processing, lower energy consumption, reduced fabrication costs, and potential for miniaturization, owing to their mechanical flexibility, optical transparency, tunable optoelectronic properties, and ease of manufacturing [10]. Reported OELGD implementations include optical switch transistors, selective light-responsive devices, organic optoelectrochemical transistors, bipolar light-responsive devices, light-responsive memory devices, multi-gate structures, and multi-mechanism coupled devices [11]. Bipolar photoresponse devices modulate carrier transport direction via internal electric fields, generating both positive and negative photocurrents. This characteristic can be achieved through various mechanisms, including photovoltaic, pyroelectric, ferroelectric, photoelectrochemical, plasmonic, or interface charge inductive effects [12–19]. Unlike traditional p–n junction diodes with unidirectional photocurrent, bipolar photoresponse enables multiple light-controlled logic operations in a single device by tuning parameters such as light wavelength, intensity, incident angle, and bias voltage [12–14]. For instance, a CdTe/SnSe photodetector (PD) demonstrated five logic gates ("AND", "OR", "NAND", "NOR", and "NOT") by controlling the dominance of photovoltaic and photothermoelectric effects within different spectral ranges [15]. Han et al. prepared a self-powered ultraviolet (UV) PD based on $BaTiO_3$(BTO)/p-GaN heterojunctions, where the bipolar photoresponse originated from reversible depolarization fields in BTO [16]. Wang et al. fabricated a t-Se/InSe heterojunction photoelectrochemical PD (PEC PD) via electrochemical deposition, exhibiting negative photocurrent under UV–visible light and positive photocurrent under near-infrared illumination due to hydrogen and oxygen evolution reactions at the interface [17]. Li et al. demonstrated a self-powered PD using Ce-doped BTO (Ce-BTO), where plasmonic resonance effects in Ag induced competitive carrier transfer, enabling wavelength-dependent photocurrent polarity switching [18]. Kim et al. designed a back-to-back p^+–i–n–p–p^+ perovskite PD in which the balance between diffusion and drift currents determined the photocurrent polarity under illumination [19]. By engineering PD structures, tailoring material microstructures, and applying external controls (e.g., light or electric fields), photocurrent polarity switching can be achieved, enabling applications in high-resolution multicolor imaging, biomedical photodetection, portable spectrometers, multi-channel optical communication, and optical logic operations [20, 21].

BiOX (X = Cl, Br, I) materials, particularly BiOI, feature Bi^{3+} cations with an ns^2 valence electron configuration, exhibiting anti-bonding orbital characteristics at the band edge. This electronic structure resembles that of perovskite $MAPbX_3$, earning BiOI the designation of a "perovskite-inspired" material [22]. BiOI possesses a unique layered structure comprising alternating $[Bi_2O_2]^{2+}$ and double I^- ion layers, demonstrating high anisotropy, defect tolerance, and optoelectronic properties [22–24]. With a theoretical bandgap of 1.9 eV and strong absorption in UV–visible regions, BiOI finds applications in photocatalysis and optoelectronic devices [25, 26]. The conduction-band of BiOI primarily consists of Bi 6p orbitals with minor contributions from I 5p and O 2p, while the valence-band arises from hybridization of I 5p and O 2p orbitals [27, 28]. Adjusting the chemical stoichiometry of BiOI enables band-structure modulation. The dispersed conduction-band energy levels and multi-peak valence-band density of states allow excitation of electrons from various valence-band states to the conduction-band under different photon energies [25].

Photons with energy near the bandgap of BiOI primarily excite electron transitions from the valence-band minimum (VBM) to the conduction-band maximum (CBM), whereas high-energy photons can additionally promote electrons from deeper valence-band states to the conduction-band. In BiOI-based heterojunctions, the deliberate design of conduction-band offset (ΔE_C) and valence-band offset (ΔE_V) enables precise modulation of photo-generated carrier states through incident photon energy control. The resulting photocurrent direction in the external circuit is determined by the competition between two key interfacial processes of electron–hole recombination and carrier tunneling.

In this study, we fabricated BiOI/TiO_2 heterojunction devices by depositing two-dimensional BiOI nanoflakes on TiO_2 thin films through a combined solvothermal and liquid-phase deposition approach. To engineer the band structure, Glycerol (GL) was introduced into the BiOI precursor solution to regulate the binding rate of I^- with BiO^+ during solvothermal reaction. This additive promotes the oxidation of I^- to I_2 precipitates, yielding iodine-deficient, bismuth-rich BiOI nanoflakes. The modified stoichiometry effectively tunes both the energy-band structure of BiOI and the interfacial band offsets (ΔE_C and ΔE_V) in the heterojunction [28]. The wavelength-dependent photocurrent polarity arises from the controlled manipulation of interfacial potential barriers, which govern the relative dominance of carrier tunneling versus recombination processes. By exploiting these dual-band bipolar photoresponse characteristics in BiOI/TiO_2 heterojunctions, we successfully implemented five fundamental logic operations ("AND", "OR", "NAND", "NOR", and "NOT") within a single device using UV and visible light as optical input signals.

The UV–visible logic functionality of this BiOI/TiO_2 heterojunction device further extends its application potential to the field of biomimetic in-sensor image processing. Specifically, it enables simulation of the unique visual system of bees, which detect UV light (300–400 nm) that is invisible to humans to recognize UV nectar guides on flower petals for foraging. This simulation is achieved by performing logic-based in-sensor processing on images of *Chrysanthemum carinatum*, a typical insect-pollinated flower with distinct UV reflection patterns. This biomimetic application not only validates the practicality of the device logic capabilities in real-world scenarios but also opens new avenues for integrating optoelectronic logic devices with biological perception mechanisms, which could contribute to advancements in fields such as biomimetic sensors, smart agriculture, and environmental imaging where detection of non-visible spectral information is critical.

2 Results and discussion

2.1 Morphology, crystal structure, and optical properties of BiOI/TiO_2 heterojunctions

Figure 1(a) shows the scanning electron microscopy (SEM) images of TiO_2 thin films grown by liquid-phase deposition. The as-grown TiO_2 films, with a thickness of approximately 370 nm, consist of densely packed shuttle-shaped particles. Figures 1(b)–1(d) present

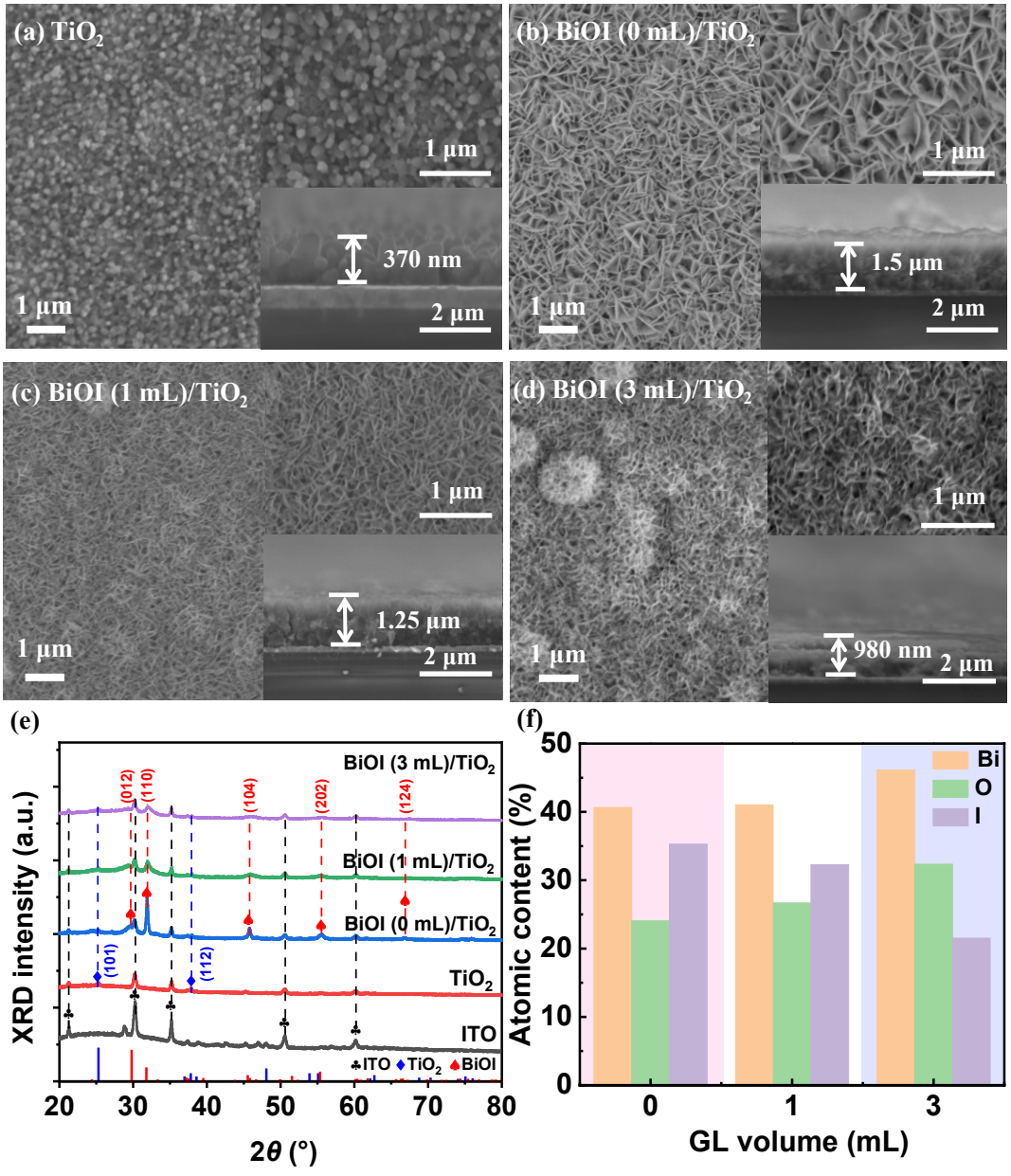


Figure 1 Top view and cross-sectional view SEM images of (a) TiO_2, (b) BiOI (0 mL)/TiO_2, (c) BiOI (1 mL)/TiO_2, and (d) BiOI (3 mL)/TiO_2 films, respectively. (e) XRD patterns of TiO_2 and BiOI/TiO_2. (f) EDS spectrum element content statistics of BiOI.

the SEM images of BiOI/TiO_2 prepared with different amounts of GL in the BiOI precursor solution. BiOI nanoflakes with a close-packed structure grow vertically on the surface of TiO_2 thin films. Individual nanoflakes have a thickness of ~ 20 nm and a lateral dimension of ~ 0.67 μm. As the amount of GL added increases, the surface smoothness of the nanoflake films decreases, which can be attributed to the reduced lateral dimension and thickness of the nanoflakes, as well as enhanced self-assembly of nanoflakes into nanospheres. The thickness of BiOI (0 mL)/TiO_2, BiOI (1 mL)/TiO_2, and BiOI (3 mL)/TiO_2 films are 1.5, 1.25, and 0.98 μm, respectively, indicating that GL addition inhibits the growth of BiOI film. Figure 1(e) presents the X-ray diffraction (XRD) patterns of TiO_2 grown on an indium-tin oxide (ITO) substrate and BiOI films deposited on TiO_2 with varying GL amounts. Apart from the diffraction peaks of the ITO substrate, the TiO_2 film exhibits peaks at 25.28° and 38.57°, corresponding to the (101) and (112) crystal planes of anatase-phase TiO_2 (PDF #21-1272), with no other phase peaks detected [29]. For BiOI/TiO_2 composite films, diffraction peaks at 29.74°, 31.73°, 45.78°, 49.91°, and 66.52° correspond to the (012), (110), (014), (202), and (124) crystal planes of BiOI (PDF #73-2062), among which the (110) plane diffraction peak is the strongest [30]. With increasing GL addition, the intensity of all BiOI diffraction peaks decreases, which is related to the reduced nanoflake thickness and likely poor crystalline quality of BiOI formed in the presence of GL.

Figure 1(f) summarizes the elemental composition analysis of BiOI films with different GL amounts, based on energy dispersive X-ray spectroscopy (EDS) spectra (Fig. S1 in the Electronic Supplementary Material (ESM)). EDS results confirm the presence of only Bi, O, and I, with no other impurities. The atomic contents of Bi, O, and I, as well as the Bi/I ratio, are listed in Fig. S1 and Table S1 in the ESM. The Bi/I ratios for BiOI (0 mL), BiOI (1 mL),

and BiOI (3 mL) films are 1:0.86, 1:0.78, and 1:0.46, respectively. The iodine content in all BiOI nanoflake films is significantly lower than the stoichiometric ratio and decreases with increasing GL addition. According to the solvothermal reaction mechanisms for BiOI formation (Eqs. (1)–(4)), I^- ions are easily oxidized to I_2 by HNO_3 (a byproduct in the reaction solution), leading to sub-stoichiometric iodine in BiOI [28]. The relevant reactions are as follows

$$2Bi(NO_3)_3 \cdot 5H_2O + 3HOCH_2CH_2OH \rightarrow Bi_2(OCH_2CH_2O)_3 + 6HNO_3 + 10H_2O \quad (1)$$

$$2Bi_2(OCH_2CH_2O)_3 + 4KI + 4H_2O \rightarrow 4BiOI\downarrow + 3HOCH_2CH_2OH + 4KOH \quad (2)$$

$$4HNO_3 \rightarrow 2H_2O + 4NO\uparrow + 3O_2\uparrow \quad (3)$$

$$8H^+ + 2NO^{3-} + 6I^- \rightarrow 3I_2 + 2NO\uparrow + 4H_2O \quad (4)$$

In the precursor solution, EG chelates with Bi^{3+} ions, inhibiting the rapid hydrolysis of $Bi(NO_3)_3{\cdot}5H_2O$. Simultaneously, HNO_3 is generated (Eq. (1)). Upon heating, the $Bi_2(OCH_2CH_2O)_3$ chelate reacts with KI and H_2O to form BiOI (Eq. (2)). At high temperatures, HNO_3 decomposes (Eq. (3)) and acts as a strong oxidizing agent, reacting with I^- to produce I_2 (Eq. (4)). According to the Stokes–Einstein equation ($D = kT/6\pi\eta r$, where D is the diffusion coefficient, k is the Boltzmann constant, T is the absolute temperature, η is the viscosity coefficient of solvent, and r is the radius of the reacting molecules), D is inversely proportional to η under constant conditions. Due to its higher viscosity, GL has a lower diffusion rate than EG at the same temperature. Thus, GL addition slows the reaction rate by limiting diffusion, reducing the concentration of I^- around BiO^+. This promotes I^- oxidation to I_2 by HNO_3, leading to decreased iodine content in BiOI with increasing GL [28, 31]. Consistently, the post-reaction solution color shifts from yellow-green to orange-red with more GL, indicating increased black solid I_2 precipitation.

X-ray photoelectron spectroscopy (XPS) was performed to analyze the surface elemental composition and valence states of TiO_2 films and BiOI films, with all spectra calibrated to C 1s (284.8 eV). Figure 2(a) shows the Ti 2p XPS spectrum of TiO_2, with two peaks at 458.2 and 464.0 eV ((binding energy difference ΔE_B = 5.8 eV), corresponding to Ti $2p_{3/2}$ and Ti $2p_{1/2}$ of Ti^{4+} in TiO_2 [32]. Figure 2(b) displays the O 1s XPS spectrum of TiO_2, which is asymmetric and has been fitted into two peaks at 529.5 eV (lattice oxygen, O_L) and 530.9 eV (oxygen vacancies related to sublattice oxygen, O_V) [33]. Figures 2(c)–2(e) depict the XPS spectra of BiOI nanoflake on TiO_2 with varying GL amounts, which are similar across samples. The Bi 4f XPS spectrum (Fig. 2(c)) has peaks at 159.04 and 164.34 eV, corresponding to Bi $4f_{7/2}$ and Bi $4f_{5/2}$ of Bi^{3+} [34]. The I 3d XPS spectrum (Fig. 2(d)) displays peaks at 618.94 and 630.34 eV, assigned to I $3d_{5/2}$ and I $3d_{3/2}$ orbits of I^- [34]. The O 1s XPS spectrum of BiOI (Fig. 2(e)) is fitted into three peaks at 529.7 eV (O_L), 531 eV (O_V), and 532.8 eV (adsorbed water/OH groups, O_H) [35]. With increasing GL, the proportion of O_L decreases, while those of O_V and O_H increase, indicating degraded crystalline quality. From the XPS valence-band (VB) spectra (Fig. 2(f)), the energy difference between the Fermi level (E_F) and VBM was determined from the tangent of the maximum slope and baseline extension. The energy difference between E_F and VBM is 2.34 eV for TiO_2, and 1.12, 1.10, and 1.06 eV for BiOI (0 mL), BiOI (1 mL), and BiOI (3 mL), respectively.

Figure 3(a) shows UV–visible absorption spectra of TiO_2 film and BiOI/TiO_2 films. TiO_2 absorbs strongly in the UV region but weakly in the visible region. BiOI deposition extends TiO_2 absorption into the visible region and enhances UV absorption. With increasing GL, the absorption edge of BiOI/TiO_2 blue-shifts. The optical bandgap (E_g) was calculated through diffuse reflectance spectra using the Kubelka–Munk function (Eq. (5)) and the Tauc relation (Eq. (6)).

$$F(R) = \frac{(1-R)^2}{2R} \quad (5)$$

$$(\alpha h\nu)^{\frac{1}{n}} = A(h\nu - E_g) \quad (6)$$

where R is the reflectance coefficient, α is the absorption coefficient, $h\nu$ is photon energy, A is a constant, and n = 1/2 (direct bandgap) or 2 (indirect bandgap). From Fig. 3(b), the bandgap of TiO_2 is approximately 3.25 eV, close to the reported value for anatase-phase TiO_2 (3.2 eV) [36]. The bandgaps of BiOI (0 mL), BiOI (1 mL), and BiOI (3 mL) are 2.26, 2.46, and 2.59 eV, respectively, slightly higher than the theoretical BiOI bandgap (1.9 eV) [37]. Theoretical calculations indicate that the VBM of BiOI is dominated by O 2p and I 5p orbitals, while its CBM involves Bi 6p, O 2p, and I 5p orbitals. In Bi-rich, I-deficient BiOI, reduced I 5p states cause the VBM to shift downward and the CBM upward, widening the bandgap [27].

Mott–Schottky (*M–S*) plots for TiO_2, BiOI (0 mL), BiOI (1 mL), and BiOI (3 mL) are illustrated in Figs. 3(c) and 3(d). The positive slope of TiO_2 and negative slope of BiOI confirm n-type and p-type behavior, respectively. The flat band potential (V_{FB}), determined from the intersection of the maximum slope tangent and baseline, represents the energy difference between the semiconductor's E_F and the Ag/AgCl reference electrode. The V_{FB} values are −0.46 eV for TiO_2, 2.38, 2.41, and 2.46 eV for BiOI (0 mL), BiOI (1 mL), and BiOI (3 mL), respectively. The E_F positions relative to the vacuum level were calculated using Eqs. (7) and (8).

$$E(\mathrm{RHE}) = E(\mathrm{Ag/AgCl}) + 0.197 + 0.0591 \times \mathrm{PH} \quad (7)$$

$$E_F = -4.5 - E(\mathrm{RHE}) \quad (8)$$

where pH = 5.8 (0.1 M Na_2SO_4 solution). E(RHE) is V_{FB}. The calculated E_F values relative to the vacuum level are −4.58 eV for TiO_2, −7.42, −7.45, and −7.50 eV for BiOI (0 mL), BiOI (1 mL), and BiOI (3 mL), respectively.

2.2 Dual-band bipolar photoresponse characteristics of BiOI/TiO_2 heterojunction PDs

The current–voltage (*I–V*) curves of Au/BiOI/TiO_2/ITO heterojunction devices in the dark and under 365 nm UV light, 420 and 475 nm visible light are shown in Figs. 4(a)–4(c). Hysteresis in dark *I–V* curves is related to the polarization properties of BiOI, confirmed by polarization–electric field (*P–E*) curves (Figs. S2(a) and S2(b) in the ESM). Illumination increases current, indicating photosensitivity of the devices. The open-circuit voltage (V_{OC}) and short-circuit current (I_{SC}) under illumination indicates the devices can operate without external bias. Figure 4(d) summarizes V_{OC} and I_{SC} for the devices with different GL amount under UV and visible

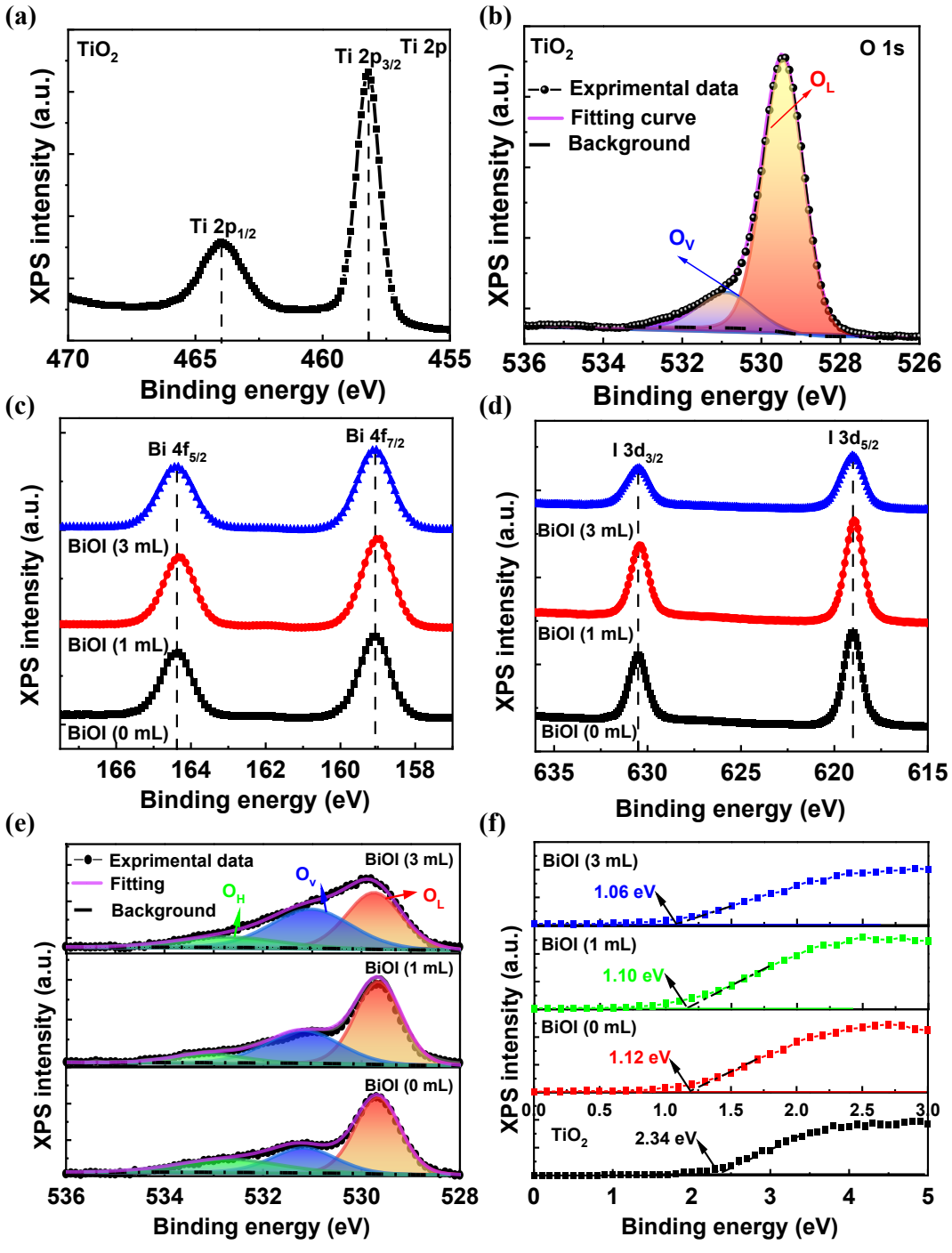


Figure 2 (a) Ti 2p and (b) O 1s XPS spectra of TiO_2 thin films. (c) Bi 4f, (d) I 3d, and (e) O 1s XPS spectra of BiOI nanoflakes deposited on TiO_2 thin films with different GL addition amounts. (f) XPS VB spectra of TiO_2 thin films and BiOI thin films.

light. The V_{OC} is generally small and higher under UV than visible light. For BiOI (0 mL)/TiO_2 device, I_{SC} values under 365, 420, and 475 nm light are −1.19, −0.28, and 0.27 nA respectively, while for the BiOI (1 mL)/TiO_2 device, the values are 0.11, −1.7, and −1 nA. The reversed I_{SC} polarity under different wavelengths indicates wavelength-tunable photocurrent direction for the BiOI (0 mL)/TiO_2 and BiOI (1 mL)/TiO_2 devices. Without external bias, both exhibit wavelength-controlled photocurrent polarity switching, achieving dual-band (UV–visible) bipolar photoresponse, whereas the BiOI (3 mL)/TiO_2 device shows unipolar behavior.

To further investigate the wavelength dependence of photocurrent polarity, photocurrents were measured at biases ranging from –0.5 to +0.5 V (Figs. 5(a)–5(c)). The results presented in these figures demonstrate that for the BiOI (0 mL)/TiO_2 device (Fig. 5(a)), the zero-bias photocurrent exhibits a negative value under UV illumination, with a maximum magnitude observed at 355 nm. Above 450 nm, polarity switches to positive, peaking at 490 nm, and the photocurrent magnitude decreases at wavelengths beyond 550 nm. A positive (negative) bias induces a blue-shift (red-shift) in the polarity switching wavelength, while also modulating

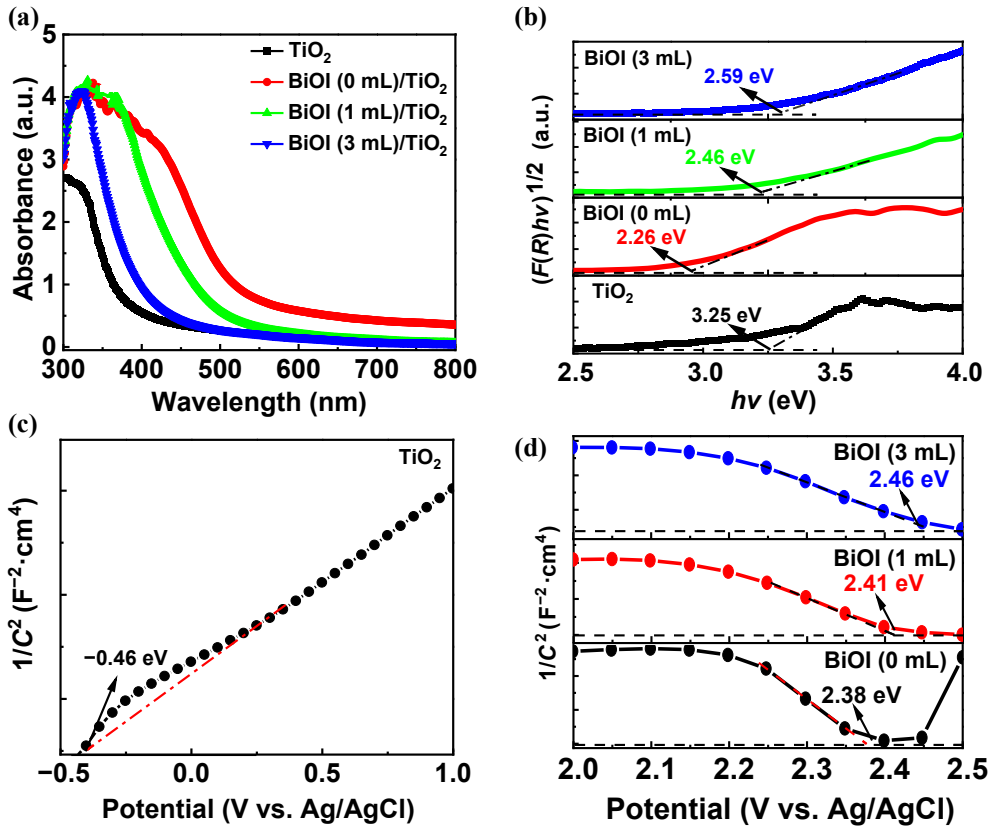


Figure 3 (a) Absorption spectra and (b) optical bandgap for TiO_2 and BiOI/TiO_2 thin films prepared with glycerol addition. *M–S* curves of (c) TiO_2 and (d) BiOI prepared with GL addition tested at 1 kHz.

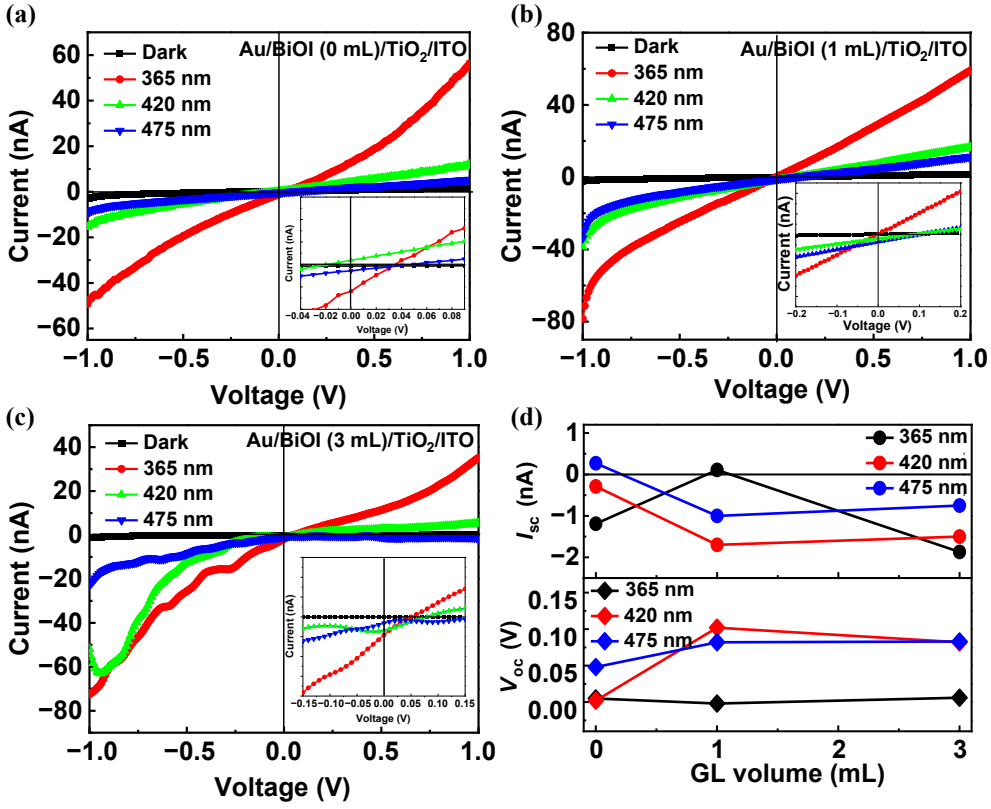


Figure 4 *I–V* curves under dark and different wavelengths illuminations for (a) BiOI (0 mL)/TiO_2, (b) BiOI (1 mL)/TiO_2, and (c) BiOI (3 mL)/TiO_2 heterojunction devices. (d) The open-circuit voltage and short-circuit current of BiOI/TiO_2 heterojunction devices under UV and visible light illuminations with the light power density of 4 mW/cm^2.

the magnitude of the photocurrent. Beyond ±0.5 V, wavelength-controlled polarity disappears, and photocurrent becomes unipolar across UV–visible ranges, with bias only affecting magnitude. Dual-band bipolar response persists at biases from −0.05 to +0.1 V. For BiOI(1 mL)/TiO_2 device (Fig. 5(b)), under high-energy UV, photocurrent is positive (maximum at 340 nm). Polarity switches at 370 nm, reaching a negative maximum at 395 nm. Positive (negative) bias enhances positive (negative) current and suppresses the opposite, but does not alter the critical switching wavelength. Bipolar response is maintained across −0.5 to +0.5 V. For BiOI (3 mL)/TiO_2 device (Fig. 5(c)), photocurrent is negative (maximum at 370 nm) at biases less than 0.05 V, exhibiting unipolar behavior. Above V_{OC}, photocurrent becomes positive, in accordance with the photovoltaic effects of heterojunction.

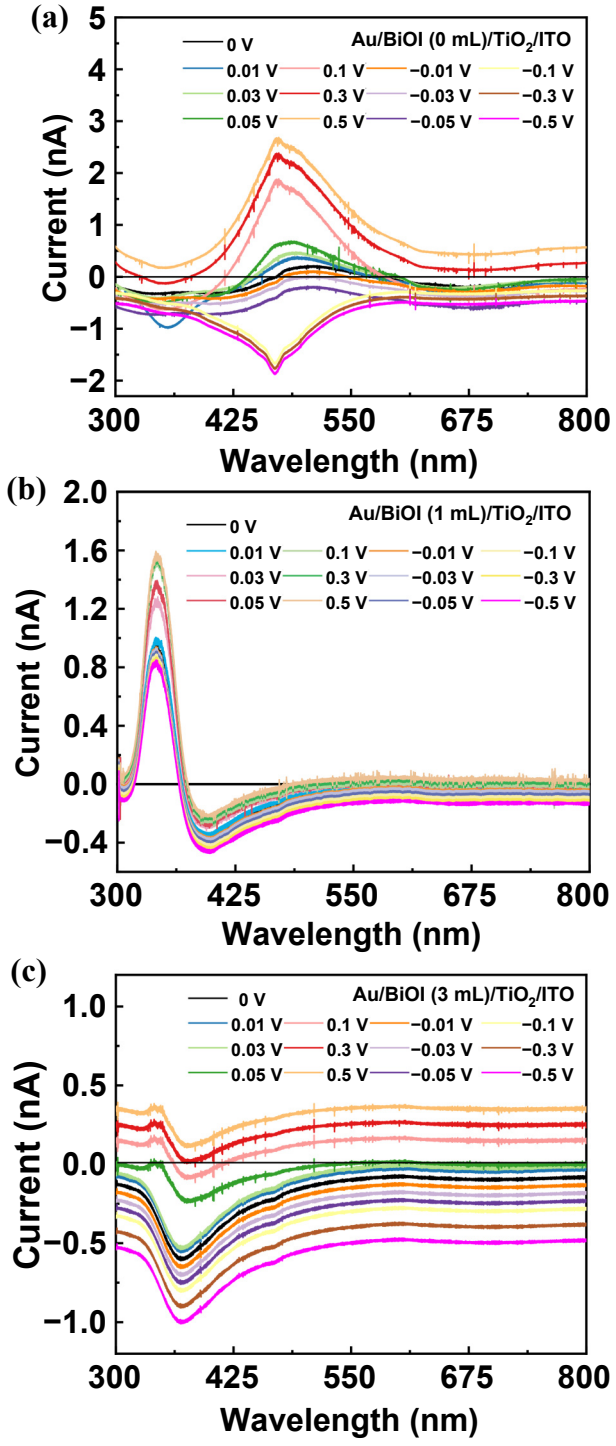


Figure 5 Photocurrent curves of (a) BiOI (0 mL)/TiO_2, (b) BiOI (1 mL)/TiO_2, and (c) BiOI (3 mL)/TiO_2 with light wavelength variation under different bias voltages.

The positions of the CBM, VBM, and E_F of TiO_2 and BiOI relative to the vacuum level are summarized in Fig. 6(a), determined from XPS VB spectra, absorption spectra, and the *M*–*S* curves. TiO_2 has a higher E_F than BiOI. Due to differing carrier concentrations, excess electrons in TiO_2 and holes in BiOI diffuse towards the interface until equilibrium, creating potential wells for BiOI electrons and TiO_2 holes. These wells hinder photogenerated electron transfer from BiOI to TiO_2 and hole transfer from TiO_2 to BiOI, promoting recombination of TiO_2 holes and BiOI electrons at the interface (processes 1 and 2 in Fig. 6).

Under UV illumination, both TiO_2 and BiOI absorb photons, generating electron–hole pairs. Theoretical calculations revealed that BiOI's valence-band has a dense, multi-peak density of states, thereby high-energy photons excite electrons from this broad distribution to the conduction-band. Under visible light (energy < TiO_2 bandgap but > BiOI bandgap), photons transmit through TiO_2 and are absorbed by BiOI. BiOI's photogenerated electrons tend to accumulate in interfacial potential wells, impeding transfer to TiO_2. UV illumination induces significant interfacial recombination of TiO_2 holes and BiOI electrons due to barriers. At low barriers, some BiOI electrons and TiO_2 holes tunnel across, transferring to TiO_2's conduction-band and BiOI's valence-band, respectively, generating negative photocurrent as charges are collected by ITO and Au. At high barriers, such tunneling is inhibited.

Figure 6(b) illustrates carrier transfer in BiOI (0 mL)/TiO_2 devices under UV irradiation. Large offsets (ΔE_C = 2.61 eV, ΔE_V = 1.62 eV) create high interfacial barriers, preventing BiOI electron and TiO_2 hole transfer. Unrecombined TiO_2 electrons and BiOI holes are collected by ITO and Au (process 1 and 4), generating negative current. As wavelength increases, TiO_2 electron generation decreases, reducing photocurrent. For visible light (energy < TiO_2 bandgap but > BiOI bandgap), photocurrent arises from BiOI (Fig. 6(c)). Electrons near the VBM are excited to the CBM, leaving holes that are captured by V_O-derived donor levels (process 7), consistent with O 1s XPS [38]. Higher-energy BiOI electrons tunnel to TiO_2 (process 5), whereas lower-energy electrons have lower tunneling probability, reducing negative current with increasing wavelength. Un-tunneled electrons move to Au and recombine with holes trapped by O_V. For λ > 470 nm, electrons near BiOI's VBM are excited, increasing trapped holes and remaining holes recombine with electrons at Au. Unrecombined electrons are collected by Au (process 6), generating small positive current (Fig. 6(d)), peaking at 490 nm (near BiOI's bandgap).

Applying positive (negative) bias to BiOI (0 mL)/TiO_2 device shifts BiOI bands downward (upward) and TiO_2 bands upward (downward), facilitating (hindering) BiOI electron and TiO_2 hole transfer to Au and ITO, while suppressing (promoting) interfacial recombination and TiO_2 electron transfer to Au. Larger bias increases band bending: positive bias reduces negative current, while negative bias enhances it (for energies << BiOI bandgap). Near the BiOI bandgap, positive (negative) bias increases (decreases) positive current, with switching wavelength blue-shifting (red-shifting). Below −0.05 V, severe band bending prevents electron collection at Au.

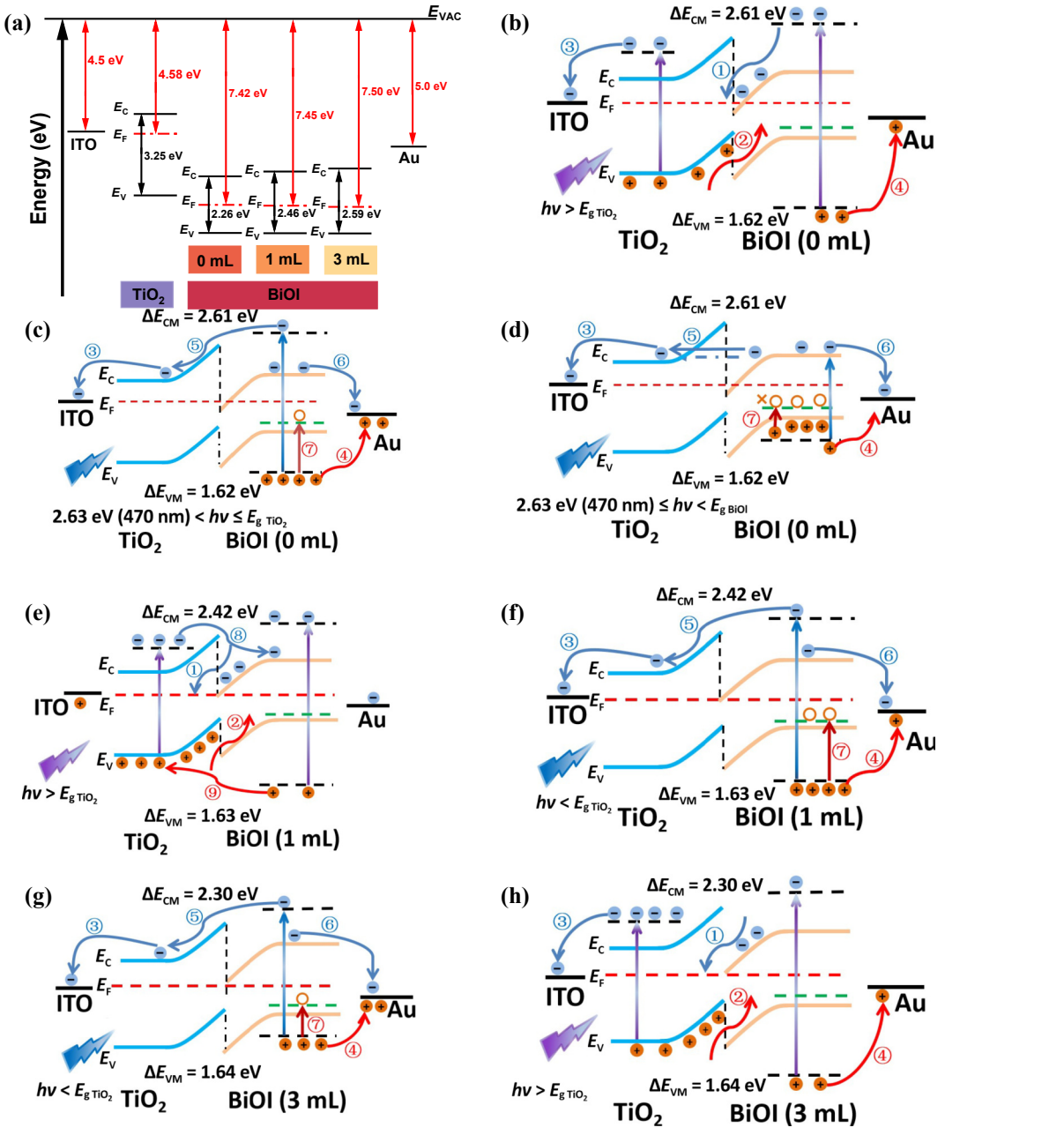


Figure 6 Energy level structure diagram: (a) before contact between BiOI and TiO_2; the BiOI (0 mL)/TiO_2 heterojunction exhibits (b) higher incident light energy than E_g of TiO_2, (c) lower than E_g of TiO_2 but much higher than E_g of BiOI, and (d) closer to E_g of BiOI. The BiOI (1 mL)/TiO_2 heterojunction exhibits (e) higher incident light energy than E_g of TiO_2 and (f) lower incident light energy than E_g of TiO_2. BiOI (3 mL)/TiO_2 has (g) a higher incident light energy than E_g of TiO_2 and (h) a lower incident light energy than E_g of TiO_2. Among them, processes 1 and 2 represent the recombination of TiO_2 holes and BiOI electrons at the interface. Process 3: the movement of electrons on the TiO_2 conduction-band towards one end of the ITO electrode. Process 4: the movement of photogenerated electrons from the conduction-band of BiOI to Au electrode. Process 5: High-energy photo-generated electrons in BiOI can be transferred to the TiO_2 through tunneling. Process 6: Electrons that have not undergone tunneling on the conduction-band of BiOI transfer to Au electrode. Process 7: Photo-generated holes are captured by the donor level formed by the V_O of BiOI. Process 8: High-energy photo-generated electrons on the TiO_2 conduction-band can tunnel through the interface barrier and transfer to the BiOI. The photogenerated electrons in the conduction-band of BiOI move towards Au electrode. Process 9: the transfer of high-energy photo-generated hole tunneling through the interface barrier on the BiOI valence-band to that of TiO_2.

Figure 6(e) shows carrier transfer in BiOI (1 mL)/TiO_2 devices under UV light. BiOI (1 mL) has a higher CBM than BiOI (0 mL) (ΔE_C = 2.42 eV). High-energy UV excites TiO_2 electrons that tunnel to BiOI's conduction-band (process 8) and are collected by Au, while high-energy BiOI holes tunnel to TiO_2's valence-band (process 9) and are collected by ITO. Interfacial recombination of BiOI electrons and TiO_2 holes also occurs. Tunneling dominance generates positive current, whereas recombination dominance generates negative current. As wavelength increases, fewer high-energy carriers form, reducing tunneling and increasing recombination, causing polarity switching at 370 nm. Under visible light (energy < TiO_2 bandgap), BiOI carriers dominate. High-energy BiOI electrons tunnel to TiO_2 (process 5), while others move to Au. Some holes are trapped by O_V (process 7), and others

recombine with electrons at Au (process 4), leaving residual holes to generate small negative current. Longer wavelengths reduce electron energy and tunneling, decreasing negative current magnitude.

For the BiOI (1 mL)/TiO_2 device, positive (negative) bias shifts BiOI bands down (up) and TiO_2 bands up (down), promoting (suppressing) TiO_2 electron and BiOI hole transfer, and suppressing (promoting) recombination, enhancing positive (negative) current. BiOI nanoflakes with varying GL have similar VBM positions, and I-deficient BiOI has a higher CBM due to reduced I 5p contribution. BiOI (3 mL)/TiO_2 has a smaller ΔE_C (2.23 eV), facilitating BiOI electron tunneling to TiO_2, but high BiOI CBM reduces TiO_2 electron tunneling to BiOI under UV. Thus, UV illumination generates negative current via TiO_2 electron collection by ITO (process 3, Fig. 6(g)) and BiOI electron tunneling to TiO_2 (process 5, Fig. 6(h)), alongside O_V-trapped hole recombination. Under visible light, weak negative current arises from residual holes collected by Au. Negative bias enhances BiOI electron tunneling, increasing negative current, whereas positive bias above V_{OC} increases diffusion current, generating positive current.

Figures S3(a)–S3(d), S4(a)–S4(d), and S5(a)–S5(d) in the ESM depict the *I*–*t* curves under 365 nm UV light, and 420 and 475 nm light (4 mW/cm^2) at 0–0.3 V and zero-bias curves under varying intensities. Figure 7 summarizes photocurrent dependence on bias, intensity, and wavelength. For BiOI (0 mL)/TiO_2 device, bias and wavelength tune current amplitude and polarity. Zero-bias current is opposite under 365 and 475 nm. Above V_{OC}, current is positive for both. For BiOI (1 mL)/TiO_2 device at 0–0.3 V, bipolar current is achieved by tuning UV–visible bands, with polarity retained across voltages. BiOI (3 mL)/TiO_2 device shows unipolar current. Zero-bias polarity is fixed, but magnitude increases with light intensity.

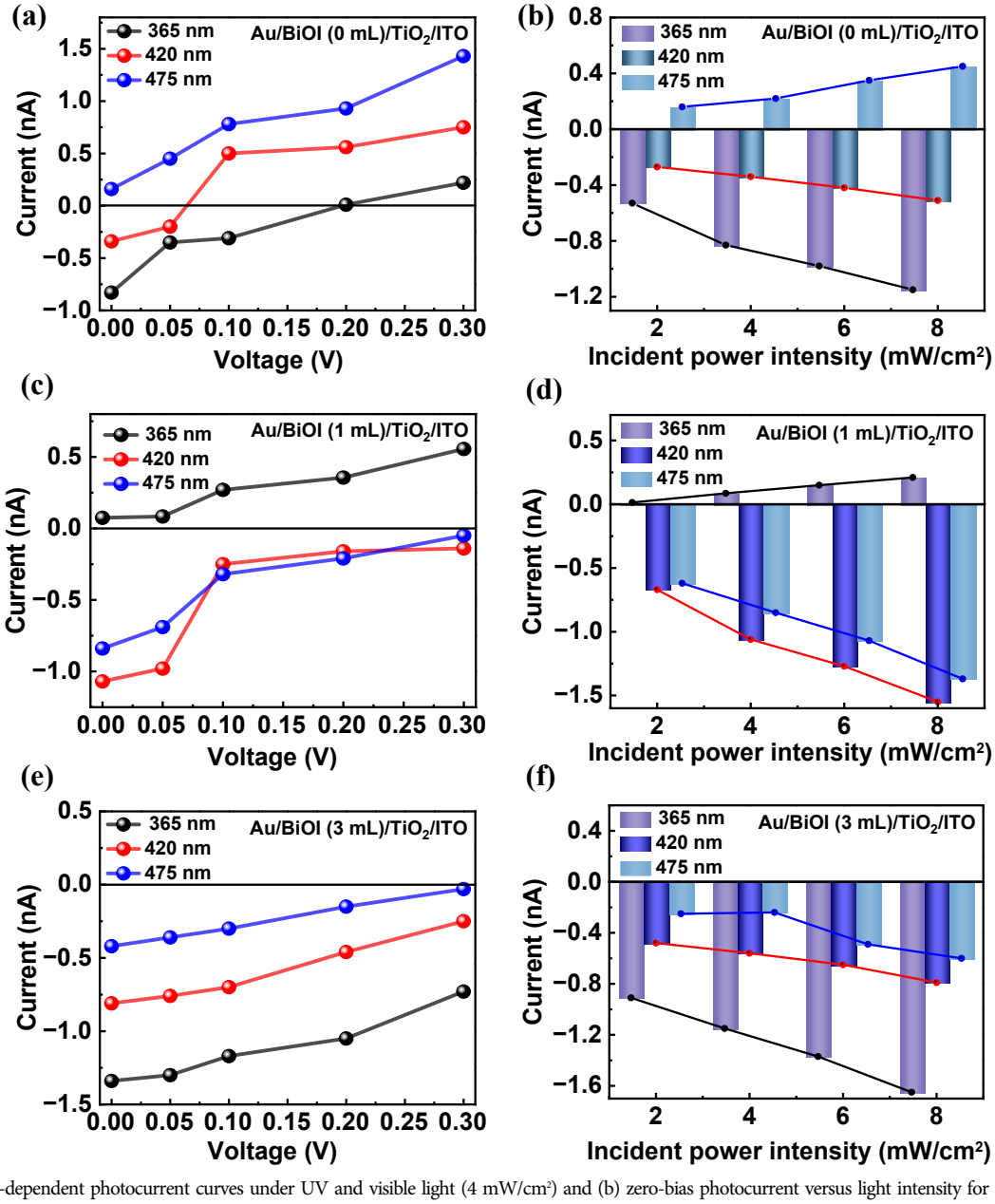


Figure 7 (a) Bias-dependent photocurrent curves under UV and visible light (4 mW/cm^2) and (b) zero-bias photocurrent versus light intensity for BiOI (0 mL)/TiO_2 heterojunction device. Corresponding plots for ((c) and (d)) BiOI (1 mL)/TiO_2 heterojunction device and ((e) and (f)) BiOI (3 mL)/TiO_2 heterojunction device.

2.3 Application of BiOI/TiO_2 heterojunction PDs in optoelectronic logic gates

The Au/BiOI (1 mL)/TiO_2/ITO device exhibits wavelength-controlled dual-band bipolar photoresponse across −0.5 to +0.5 V, with current magnitude tunable by bias and light intensity. Using 365 nm UV and 475 nm visible light are used as inputs, five basic logic gates ("AND", "OR", "NAND", "NOR", and "NOT") are realized by controlling voltage and light intensity. The truth table and schematic diagram for the logic operation of optical signals are presented in Table 1 and Fig. 8(a), respectively. The logic operations involved are defined as follows: "1" denotes light on, "0" denotes light off; "11" denotes both lights are on, "00" denotes both lights are off, and "10"/"01" denotes only one light is on. The threshold current is −0.1 nA, where the output is defined as "1" for current > threshold, "0" otherwise [39]. Figures 8(b)–8(f) demonstrate the implementation of "AND", "OR", "NAND", "NOR", and "NOT" logic gates using the regulated output photocurrent of the Au/BiOI (1 mL)/TiO_2/ITO device, achieved by controlling the operating voltage and light intensity. The "AND" logic gate is realized at zero bias under 365 nm UV light (0.13 mW/cm^2) and 475 nm visible light (0.8 mW/cm^2) illuminations. When the input light signals are in "00", "01", or "10", the output photocurrent remains below the threshold, resulting in an output signal of "0". Conversely, when the input is in "11", the photocurrent exceeds the threshold, yielding an output

Table 1 Double-valued logic gate truth table

Input-light		Output-logic				
L_1 (365 nm)	L_2 (475 nm)	AND	OR	NAND	NOR	NOT
0	0	0	0	1	1	1
0	1	0	1	1	0	0
1	0	0	1	1	0	—
1	1	1	1	0	0	—

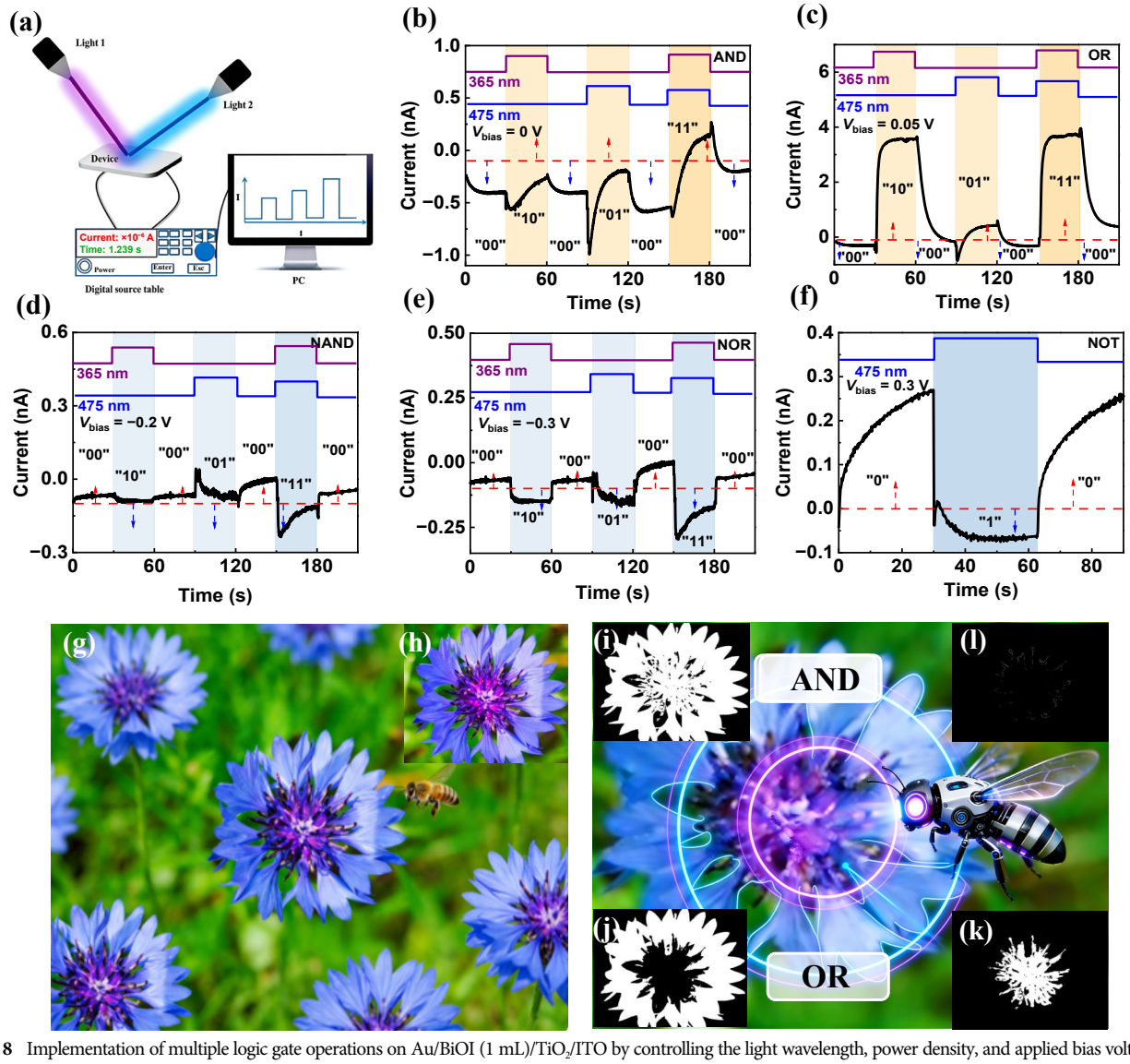


Figure 8 Implementation of multiple logic gate operations on Au/BiOI (1 mL)/TiO_2/ITO by controlling the light wavelength, power density, and applied bias voltage. (a) operation schematic diagram, (b) "AND" gate, (c) "OR" gate, (d) "NAND" gate, (e) "NOR" gate, and (f) "NOT" gate. Implementation of in-sensor logic processing for images: (g) the UV nectar guides of *Chrysanthemum carinatum* (for bees); (h) original image; (i) dual-channel grayscale extraction; (j) the "OR" logic with a blue light input of "1" and a UV light input of "0"; (k) the "OR" logic with a blue light input of "0" and a UV light input of "1"; (l) the "AND" logic with a blue light input of "1" and a UV light input of "1".

of "1" thereby fulfilling the "AND" logic operation. The "OR" logic gate is achieved at 0.05 V bias under 365 nm UV light (1.2 mW/cm^2) and 475 nm visible light (1.7 mW/cm^2) illumination. Here, the output signal is "1" for input states "01", "10", or "11", where the photocurrent surpasses the threshold. Only when both inputs are "00" does the output register as "0". The "NAND" and "NOR" logic gates are implemented by leveraging the device's dark current under negative bias, which exceeds the photogenerated current. For the "NAND" gate (at −0.2 V bias, 365 nm UV light (0.08 mW/cm^2) and 475 nm visible light (0.23 mW/cm^2), the output is "1" for input combinations "00", "01", or "10", while the "11" input induces the photocurrent to drop below the threshold, producing a "0" output. The "NOR" gate (at −0.3 V bias, same light conditions as "NAND") yields a "0" output for inputs "01", "10" or "11" with only the "00" input resulting in an output above the threshold. The "NOT" logic gate is accomplished by utilizing the dark current under a positive bias (0.3 V). Under 475 nm visible light (4 mW/cm^2), the output photocurrent remains below the threshold, meaning the output is "1" when the input is "0" and vice versa. The results demonstrate five logic gates in a single device. The BiOI/TiO_2 heterojunction device, leveraging wavelength-tunable bipolar photocurrent via interfacial carrier tunneling and recombination, shows promise for optical logic and multi-channel communication [40]. Performance comparisons with typical optoelectronic logic gate devices are provided in Table S2 in the ESM.

In the field of image processing, the application of logic gates ("AND", "OR", "NAND", "NOR", and "NOT") primarily relies on Boolean operations performed on binary images (in which pixel values are restricted to 0 or 1). The core of this approach is to process the "valid regions (1)" and "invalid regions (0)" within an image following specific logical rules, thereby enabling functions such as region extraction, merging, and exclusion [41]. Beyond the artificial domain of image processing, biological visual systems exhibit naturally evolved light-responsive logic-like behaviors, a typical example being the visual system of bees. Their compound eyes consist of approximately 6000 ommatidia, each containing photoreceptors (cone cells) capable of detecting UV light (300–400 nm), blue light (400–500 nm), and green light (500–600 nm) [42]. By contrast, red light within the human-visible wavelength range (620–750 nm) is perceived as non-visible light by bees. Flowering plants have developed a corresponding adaptive trait: the petals reflect specific UV light patterns that form UV nectar guides. These patterns are undetectable to the human eye, but appear as distinct "targets", "stripes", or "spots" in bee vision, directly guiding bees to nectar sources (see Fig. 8(g)) [42].

To mimic this biologically optimized light-dependent recognition mechanism, the present study leverages the UV–visible logic functionality of the fabricated device to realize in-sensor processing of images of *Chrysanthemum carinatum* (common name: cornflower), a typical insect-pollinated flower. Its co-evolution with pollinators including bees is notably reflected in its UV light reflection traits: the petals not only reflect specific wavelengths of UV light, but also form a cryptic UV pattern that acts as a critical visual signal to guide bees toward efficient foraging and successful pollination. Figures 8(g) and 8(h) present a photograph of *Chrysanthemum carinatum*, while the image in Fig. 8(i) was obtained via dual-channel grayscale extraction under UV light and blue light. For blue single-channel grayscale extraction, the result corresponding to the "OR" logic (with a blue light input of "1" and a UV light input of "0") is shown in Fig. 8(j). For UV single-channel grayscale extraction, the result when corresponding to the "OR" logic with a UV light input of "1" and a blue light input of "0" is illustrated in Fig. 8(k). The result of the "OR" logic operation with both UV and blue light inputs set to "1" corresponds to the original image shown in Fig. 8(k). Figure 8(l) illustrates the result of the AND logic operation with simultaneous input of both light beams, which corresponds to the overlapping region of blue and UV light. In contrast, for the AND logic operation, no image output is generated under either single-light input or the absence of both light beams.

3 Conclusion

In summary, BiOI/TiO_2 heterojunction devices were fabricated by depositing two-dimensional layered BiOI nanoflakes onto TiO_2 films via a solvothermal method. By tuning the glycerol content in the precursor solution, iodine-deficient BiOI with adjustable conduction and valence-band positions was obtained, enabling precise control over the interfacial band offsets. The polarity of the photocurrent under different illumination wavelengths is governed by the competition between interfacial carrier tunneling and recombination. Within a bias range of −0.5 to +0.5 V, the BiOI (1 mL)/TiO_2 device exhibits wavelength-tunable bipolar photoresponse across the UV–visible spectrum. Using UV and visible light as optical inputs, five fundamental logic gates ("AND", "OR", "NAND", "NOR", and "NOT") were successfully demonstrated in a single device. These findings not only deepen the understanding of interfacial carrier dynamics in oxide heterojunctions but also pave the way for next-generation reconfigurable optoelectronic logic systems and intelligent biomimetic sensory applications.

4 Experimental

4.1 Film growth and device fabrication

ITO substrate were sequentially cleaned with detergent, acetone, isopropanol, and anhydrous ethanol sequentially, followed by drying in an oven at 80 °C. Anatase-phase TiO_2 film were grown on the cleaned ITO substrates via liquid-phase deposition. Specifically, 0.1069 g ammonium hexafluorotitanate ($(NH_4)_2TiF_6$, 99.8%) was dissolved in 15 mL ultrapure water, and 0.1002 g boric acid (H_3BO_3, 99.99%) was dissolved in 45 mL ultrapure water. Both solution were stirred at 400 rpm for 10 min. Subsequently, the boric acid solution was poured into the ammonium hexafluorotitanate solution, and the mixture was stirred at 400 rpm for 10 min. The pH of the resulting solution was adjusted to 2 by the addition of concentrated hydrochloric acid (HCl, 37 wt.%). The ITO substrates were vertically immersed in this solution for the growth of anatase-phase TiO_2 films at 75 °C for 6 h. The films were then rinsed with deionized water and air-dried.

BiOI nanoflakes films were deposited on the anatase-phase TiO_2 film via a solvothermal method to form BiOI/TiO_2 heterojunctions. Firstly, 0.9701 g bismuth nitrate pentahydrate ($Bi(NO_3)_3{\cdot}5H_2O$, 99.0%) was dissolved in a mixed solvent consisting of x (x = 0, 1, 3) mL GL (99.0%) and (30 − x) mL ethylene glycol (EG, 99.5%). Separately, 0.664 g potassium iodide (KI, 99.0%) was dissolved in 10 mL ethanol. The KI solution was then poured into $Bi(NO_3)_3{\cdot}5H_2O$ solution, and the mixture was stirred for 2 h. The TiO_2-coated substrates were immersed in the reaction solution, which was then transferred to an autoclave for reaction at 160 °C

for 10 h. After rinsing and drying, BiOI/TiO_2 heterojunction films were obtained. These films were denoted as BiOI (0 mL)/TiO_2, BiOI (1 mL)/TiO_2, and BiOI (3 mL)/TiO_2 based on the volume of GL added. Finally, Au electrodes (area: 0.04 cm^2) were sputtered onto BiOI/TiO_2 heterojunction films using a shadow mask.

4.2 Characterization and measurements

The morphology and microstructure of the samples were characterized using a SEM (Hitachi S-8010) and an XRD (Rigaku D/max 2500/PC). EDS (Model 550i) was used to analyze the elemental composition and relative contents of the BiOI films. XPS (Thermo ESCALAB-250) was employed to analyze the elemental composition, chemical states, and valence states of the samples. UV–visible absorption spectra were measured using a UV–vis spectrophotometer (Hitachi V4100). *M–S* curves were obtained with a three-electrode electrochemical workstation (Autolab PGSTAT 128N). *P–E* curves of the materials under a polarizing field were measured using a ferroelectric tester (Precision Premier II, Radiant Technologies Inc). *I–V* curves, transient photocurrent (*I–t*) responses, and wavelength-dependent photocurrent (*I–λ*) spectra were measured using Keithley 4200 and Keithley 2450 source meters. Monochromatic light of different wavelengths was provided by light-emitting diodes (LEDs).

Electronic Supplementary Material: Supplementary material (EDS spectra, *P–E* curves, additional optoelectronic properties, and performance comparison) is available in the online version of this article at https://doi.org/10.26599/NR.2026.94908701.

Data availability

All data needed to support the conclusions in the paper are presented in the manuscript and the Electronic Supplementary Material. Additional data related to this paper may be requested from the corresponding author upon request.

Acknowledgments

This work was supported by the National Natural Science Foundation of China (Nos. 52271187, 62375205, 51971158, and 51871167) and the Natural Science Foundation of Tianjin (No. 18JCYBJC86200).

Declaration of competing interest

All the contributing authors report no conflict of interests in this work.

Author contribution statement

J. P. X.: Writing – review & editing, investigation, formal analysis, data curation, conceptualization, funding acquisition. H. Y. A.: Original draft, investigation, formal analysis, data curation. S. B. S.: Investigation, formal analysis, data curation. L. N. K.: Investigation, formal analysis. X. S. Z.: Investigation, formal analysis. L. L.: Supervision, resources, funding acquisition.

Use of AI statement

None.

References

[1] Yao, J. D.; Yang, G. W. All-2D architectures toward advanced electronic and optoelectronic devices. *Nano Today* **2021**, *36*, 101026.
[2] Hu, X. Y.; Tan, T.; Chen, Y. H.; Yan, Z. M. Spatially programmable origami networks enable high-density mechanical computing for autonomous robotics. *Nat. Commun.* **2025**, *16*, 10209.
[3] Qi, Z. H.; Zhou, B.; Yan, D. P. Recent advances on molecule-based micro/nanocrystal heterojunctions for optical applications. *Adv. Opt. Mater.* **2023**, *11*, 2200852.
[4] Jiao, S. M.; Liu, J. W.; Zhang, L. W.; Yu, F. H.; Zuo, G. M.; Zhang, J. M.; Zhao, F.; Lin, W. H.; Shao, L. Y. All-optical logic gate computing for high-speed parallel information processing. *Opto-Electron. Sci.* **2022**, *1*, 220010.
[5] Yang, Y. S.; Wang, K. Z.; Yan, D. P. Smart luminescent coordination polymers toward multimode logic gates: Time-resolved, tribochromic and excitation-dependent fluorescence/phosphorescence emission. *ACS Appl. Mater. Interfaces* **2017**, *9*, 17399–17407.
[6] Wu, J. M.; Lin, X.; Guo, Y. C.; Liu, J. W.; Fang, L.; Jiao, S. M.; Dai, Q. H. Analog optical computing for artificial intelligence. *Engineering* **2022**, *10*, 133–145.
[7] Liu, J.; Wu, Q. H.; Sui, X. B.; Chen, Q.; Gu, G. H.; Wang, L. P.; Li, S. C. Research progress in optical neural networks: Theory, applications and developments. *PhotoniX* **2021**, *2*, 5.
[8] Singh, P.; Tripathi, D. K.; Jaiswal, S.; Dixit, H. K. All-optical logic gates: Designs, classification, and comparison. *Adv. Opt. Technol.* **2014**, *2014*, 275083.
[9] Zeng, S. Q.; Zhang, Y.; Li, B. J.; Pun, E. Y. B. Ultrasmall optical logic gates based on silicon periodic dielectric waveguides. *Photonics Nanostruct. Fundam. Appl.* **2010**, *8*, 32–37.
[10] Zhang, X. L.; Li, J.; Yang, W. J.; Leng, B.; Niu, P. J.; Jiang, X.; Liu, B. D. High-performance flexible ultraviolet photodetectors based on AZO/ZnO/PVK/PEDOT: PSS heterostructures integrated on human hair. *ACS Appl. Mater. Interfaces* **2019**, *11*, 24459–24467.
[11] Jeon, Y.; Kim, S.; Seo, J.; Yoo, H. Contributions of light to novel logic concepts using optoelectronic materials. *Small Methods* **2024**, *8*, 2300391.
[12] Kumar, M.; Lim, J.; Kang, H.; Kim, S.; Seo, H. Photon-triggered self-powered all electronics with graphene-silicon hybrid device. *Nano Energy* **2021**, *82*, 105668.
[13] Wang, S.; Pan, X.; Lyu, L. Y.; Wang, C. Y.; Wang, P. F.; Pan, C.; Yang, Y. K.; Wang, C.; Shi, J. W.; Cheng, B. et al. Nonvolatile Van Der Waals heterostructure phototransistor for encrypted optoelectronic logic circuit. *ACS Nano* **2022**, *16*, 4528–4535.
[14] Huang, Y.; Duan, X. F.; Cui, Y.; Lauhon, L. J.; Kim, K. H.; Lieber, C. M. Logic gates and computation from assembled nanowire building blocks. *Science* **2001**, *294*, 1313–1317.
[15] Liu, G. C.; Guo, F. H.; Zhang, M. C.; Liu, Y. J.; Hao, J. Y.; Yu, W. Z.; Li, S. Q.; Hu, B.; Zhang, B.; Hao, L. Z. All-in-one optoelectronic logic gates enabled by bipolar spectral photoresponse of CdTe/SnSe heterojunction. *ACS Appl. Mater. Interfaces* **2023**, *15*, 29375–29383.
[16] Han, W. S.; Liu, K. W.; Yang, J. L.; Zhu, Y. X.; Cheng, Z.; Chen, X.; Li, B. H.; Liu, L.; Shen, D. Z. $BaTiO_3$/p-GaN/Au self-driven UV photodetector with bipolar photocurrent controlled by ferroelectric polarization. *Chin. Phys. B* **2024**, *33*, 047701.
[17] Wang, Y. X.; Zhang, A. Q.; Liu, J. M.; Zhou, J. X.; Shao, Z. T.; Hu, P. A.; Feng, W. Mosaic Se/InSe heterojunction for self-powered bipolar photodetection. *Adv. Opt. Mater.* **2024**, *12*, 2302149.
[18] Li, C. X.; Chen, C.; Zhao, L.; Ma, N. Self-powered bipolar photodetector based on a Ce–$BaTiO_3$ PTCR semiconductor for logic gates. *ACS Appl. Mater. Interfaces* **2023**, *15*, 23402–23411.
[19] Kim, W.; Kim, H.; Yoo, T. J.; Lee, J. Y.; Jo, J. Y.; Lee, B. H.; Sasikala, A. A.; Jung, G. Y.; Pak, Y. Perovskite multifunctional logic gates via bipolar photoresponse of single photodetector. *Nat. Commun.* **2022**, *13*, 720.
[20] Purusothaman, Y.; Alluri, N. R.; Chandrasekhar, A.; Venkateswaran,

V.; Kim, S. J. Piezophototronic gated optofluidic logic computations empowering intrinsic reconfigurable switches. *Nat. Commun.* **2019**, *10*, 4381.

[21] Cheng, W. J.; Wu, S. L.; Lu, J. Y.; Li, G. Y.; Li, S. H.; Tian, W.; Li, L. Self-powered wide-narrow bandgap-laminated perovskite photodetector with bipolar photoresponse for secure optical communication. *Adv. Mater.* **2024**, *36*, 2307534.

[22] Hoye, R. L. Z.; Lee, L. C.; Kurchin, R. C.; Huq, T. N.; Zhang, K. H. L.; Sponseller, M.; Nienhaus, L.; Brandt, R. E.; Jean, J.; Polizzotti, J. A. et al. Strongly enhanced photovoltaic performance and defect physics of air-stable bismuth oxyiodide (BiOI). *Adv. Mater.* **2017**, *29*, 1702176.

[23] Rondiya, S. R.; Jagt, R. A.; MacManus-Driscoll, J. L.; Walsh, A.; Hoye, R. L. Z. Self-trapping in bismuth-based semiconductors: Opportunities and challenges from optoelectronic devices to quantum technologies. *Appl. Phys. Lett.* **2021**, *119*, 220501.

[24] Li, T. S.; Luo, S. L.; Wang, X. J.; Zhang, L. J. Alternative lone-pair ns^2-cation-based semiconductors beyond lead halide perovskites for optoelectronic applications. *Adv. Mater.* **2021**, *33*, 2008574.

[25] Wang, Q. Y.; Liu, Z. Y.; Feng, H.; Jin, R.; Zhang, S. H.; Gao, S. M. Engineering Bi_2S_3/BiOI p-n heterojunction to sensitize TiO_2 nanotube arrays photoelectrodes for highly efficient solar cells and photocatalysts. *Ceram. Int.* **2019**, *45*, 3995–4002.

[26] Jagt, R. A.; Bravić, I.; Eyre, L.; Gałkowski, K.; Borowiec, J.; Dudipala, K. R.; Baranowski, M.; Dyksik, M.; Van De Goor, T. W. J.; Kreouzis, T. et al. Layered BiOI single crystals capable of detecting low dose rates of X-rays. *Nat. Commun.* **2023**, *14*, 2452.

[27] Wang, M. M.; Gao, J. Z.; Zhu, G. Q.; Li, N.; Zhu, R. L.; Wei, X. M.; Liu, P.; Guo, Q. M. One-step solvothermal synthesis of Fe-doped BiOI film with enhanced photocatalytic performance. *RSC Adv.* **2016**, *6*, 106615–106624.

[28] Dai, G. P.; Yu, J. G.; Liu, G. Synthesis and enhanced visible-light photoelectrocatalytic activity of p–n junction BiOI/TiO_2 nanotube arrays. *J. Phys. Chem. C* **2011**, *115*, 7339–7346.

[29] Lei, C. X.; Huang, X.; Liu, X.; Wang, L. S.; Zhang, G. S.; Peng, D. L. Photoelectrochemical performances of the SnO_2–TiO_2 bilayer composite films prepared by a facile liquid phase deposition method. *J. Alloys Compd.* **2017**, *692*, 227–235.

[30] Tian, R. W.; Liu, D.; Wang, J. Q.; Zhou, J.; Nie, E.; Piao, X. Q.; Sun, Z. Three-dimensional BiOI/TiO_2 heterostructures with photocatalytic activity under visible light irradiation. *J. Porous Mater.* **2018**, *25*, 1805–1812.

[31] Tanev, P. T.; Chibwe, M.; Pinnavaia, T. J. Titanium-containing mesoporous molecular sieves for catalytic oxidation of aromatic compounds. *Nature* **1994**, *368*, 321–323.

[32] Lei, C. X.; Zhou, H.; Feng, Z. D. Effect of liquid-phase-deposited parameters on the photogenerated cathodic protection properties of TiO_2 films. *J. Alloys Compd.* **2012**, *542*, 164–169.

[33] Maki, H.; Okumura, Y.; Ikuta, H.; Mizuhata, M. Ionic equilibria for synthesis of TiO_2 thin films by the liquid-phase deposition. *J. Phys. Chem. C* **2014**, *118*, 11964–11974.

[34] Zhao, Q.; Hao, L.; Li, F.; Liu, T. Y.; He, Y. Q.; Yang, J.; Zhang, Y. F.; Lu, Y. Piezo/photocatalytic activity of flexible BiOCl–BiOI films immobilized on SUS304 wire mesh. *J. Water Process Eng.* **2021**, *42*, 102105.

[35] Li, Y. P.; Wang, Q.; Huang, L. Y.; Xu, X. Q.; Xie, M.; Wang, H.; Huang, S. Q.; Zhang, F.; Zhao, Z. Y.; Yang, J. Enhanced LED-light-driven photocatalytic antibacterial by g-C_3N_4/BiOI composites. *J. Mater. Sci.: Mater. Electron.* **2019**, *30*, 2783–2794.

[36] Gutiérrez-Tauste, D.; Domènech, X.; Casañ-Pastor, N.; Ayllón, J. A. Characterization of methylene blue/TiO_2 hybrid thin films prepared by the liquid phase deposition (LPD) method: Application for fabrication of light-activated colorimetric oxygen indicators. *J. Photochem. Photobiol. A: Chem.* **2007**, *187*, 45–52.

[37] Bai, Y. J.; Bai, H. Y.; Qu, K. G.; Wang, F. G.; Guan, P.; Xu, D. B.; Fan, W. Q.; Shi, W. D. *In-situ* approach to fabricate BiOI photocathode with oxygen vacancies: Understanding the N_2 reduced behavior in photoelectrochemical system. *Chem. Eng. J.* **2019**, *362*, 349–356.

[38] Dai, W. W.; Zhao, Z. Y. Structural and electronic properties of low-index stoichiometric BiOI surfaces. *Mater. Chem. Phys.* **2017**, *193*, 164–176.

[39] Zheng, Q.; Xu, J. P.; Li, J.; Shi, S. B.; Chen, J.; Xu, J. H.; Kong, L. N.; Zhang, X. S.; Li, L. Regulation of Bi_2O_3 phase structure improves the self-powered UV-blue dual-band photoresponse of Bi_2O_3/TiO_2 photodetectors and the imaging application. *Surf. Interfaces* **2024**, *44*, 103758.

[40] Long, M. S.; Wang, P.; Fang, H. H.; Hu, W. D. Progress, challenges, and opportunities for 2D material based photodetectors. *Adv. Funct. Mater.* **2019**, *29*, 1803807.

[41] Abiri, E.; Darabi, A.; Salem, S. Design of multiple-valued logic gates using gate-diffusion input for image processing applications. *Comput. Electr. Eng.* **2018**, *69*, 142–157.

[42] Dyer, A. G.; Paulk, A. C.; Reser, D. H. Colour processing in complex environments: Insights from the visual system of bees. *Proc. R. Soc. B* **2011**, *278*, 952–959.

This is an open access article under the terms of the Creative Commons Attribution 4.0 International License (CC BY 4.0, https://creativecommons.org/licenses/by/4.0/).

© The Author(s) 2026. Published by Tsinghua University Press.